Proceedings of the 21st ICSMGE, Vienna, Austria, 14 – 19 June 2026. Pistrol, Adam & Schweiger (eds.)
Published by: ÖGG, Austrian Society for Geomechanics, Salzburg, Austria, ISBN 978-3-9503898-4-5
https://doi.org/10.53243/ICSMGE2026-2380

Constant-volume cyclic shear characteristics and anisotropy of granular assemblies simulating fine sand

Yohta Chiba, Takayuki Shibata, Akiyoshi Kamura, Shotaro Yamada
Department of Civil and Environmental Engineering, Tohoku University, Sendai, Japan, kamura@tohoku.ac.jp

ABSTRACT: Anisotropy in fine sands has been attributed to either loading history or depositional structure. To elucidate the fundamental mechanisms underlying such anisotropy, with particular emphasis on the influence of residual strain induced by constant-volume cyclic shear loading, numerical experiments were conducted using a three-dimensional discrete element method (DEM). A series of element simulations was performed, encompassing constant-volume cyclic shear, subsequent reconsolidation, and monotonic shear loading. The microscopic behavior of particles during cyclic shear was analyzed, and the effect of residual shear strain on the development of anisotropy during reconsolidation was evaluated. During cyclic loading, the proportions of particle rotation and sliding were computed for all particles. In regions of low effective stress, rotation was found to be more dominant than sliding. As the shear stress recovered, a stable contact network was re-established, maintaining a consistent ratio of rotation to sliding. Monotonic shear under constant volume conditions was then applied to specimens reconsolidated with varying levels of residual shear strain. The results indicated that anisotropy evolved continuously and systematically with the magnitude of residual strain. When the direction of external force coincided with the direction of concentrated inter-particle contacts, the specimen exhibited greater strength.

KEYWORDS: DEM, anisotropy, liquefaction, constant-volume cyclic shear, reconsolidation.

1 INTRODUCTION

Applications of the discrete element method (DEM) have provided useful insights into the microscopic behavior of soil particles. Jiang et al. (2021) conducted three-dimensional DEM simulations of constant volume cyclic shear tests on fine sand, capturing the occurrence of liquefaction. Their study demonstrated differences in liquefaction susceptibility under various loading modes based on changes in particle coordination number. Yang et al. (2022) carried out similar simulations and quantitatively assessed the evolution of contact structures during shear stress recovery, confirming that shear stress was restored through the mechanism of cyclic mobility.

The anisotropy of fine sand has been shown to influence its undrained cyclic shear behavior. Yamada et al. (2010) investigated the relationship between re-liquefaction resistance and anisotropy by conducting undrained monotonic shear tests on specimens reconsolidated after experiencing varying levels of residual strain during liquefaction in undrained cyclic triaxial tests. Their results indicated that anisotropy developed continuously during the liquefaction process and persisted after reconsolidation, resulting in direction-dependent variation in liquefaction resistance during subsequent shearing. Furthermore, Yamada et al. (2023) used a hollow cylinder apparatus to show that anisotropy caused by shear history significantly affects the mechanical behavior of fine sand under a wide range of stress conditions. However, due to the limitations of laboratory observation, the mechanism underlying the development of such induced anisotropy remains unclear.

In the present work, constant-volume cyclic and monotonic shear simulations were performed using DEM. Contact parameters were assigned based on mechanical principles to reproduce the undrained cyclic shear behavior of fine sand. The resulting data were used to examine the mechanisms of cyclic mobility during cyclic loading and the development of anisotropy during monotonic shearing, with a focus on microscopic inter-particle contact behavior.

2 OVERVIEW OF NUMERICAL EXPERIMENTS

2.1 *Boundary conditions and experimental procedures*

The numerical analyses were performed using PFC3D (Itasca, 2024). As illustrated in Figure 1, periodic boundary conditions were applied to the lateral boundaries to simulate a horizontally layered ground, while clump walls composed of bonded particles were placed at the top and bottom boundaries. The granular assembly consisted of spherical particles with a density of 2.656 Mg/m³, corresponding to that of Toyoura sand. Three particle sizes were used to represent the particle size distribution of Toyoura sand, and the initial void ratio prior to consolidation was set to 0.743.

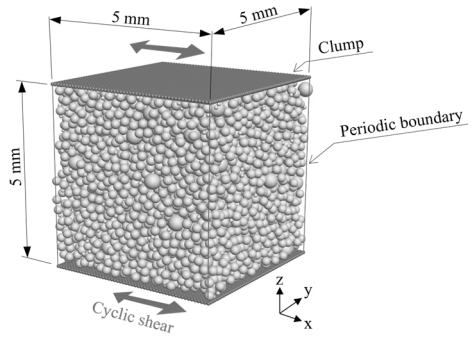

Figure 1. Initial and boundary conditions of granular specimen.

The simulation sequence consisted of consolidation, cyclic shear, reconsolidation, and monotonic shear, all conducted under zero-gravity conditions. Both consolidation and reconsolidation were carried out by applying strain-rate-controlled movements to the boundaries, thereby maintaining isotropic stress conditions. During cyclic and monotonic shear phases, simple shear deformation was imposed by moving the top and bottom clump walls in opposite directions along the x-axis under strain-rate control. The vertical movement of the clump walls was fixed to maintain constant volume conditions. The combination of zero gravity and constant volume conditions implies that the effective stress corresponds directly to the inter-particle contact forces, based on the assumption that the pore water is both incompressible and fully saturates the granular skeleton.

To represent the rotational resistance of angular fine sand using spherical particles, the rolling resistance linear model (Iwashita and Oda, 1998; Itasca, 2024) was employed for the inter-particle contact formulation.

2.2 *Inter-particle contact formulation*

As illustrated in Figure 2, the rolling resistance linear model consists of a linear spring and dashpot in the normal direction, a linear spring, dashpot, and slider in the tangential direction,

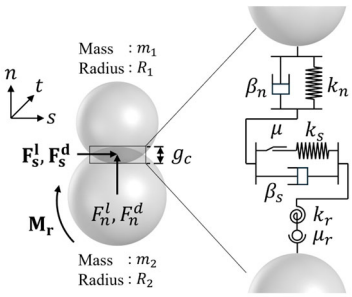

Figure 2. Overview of the rolling resistance linear model.

and a rotational spring and rotational slider for moment resistance. The total normal force F_n is computed as the sum of the normal component of the linear force F_n^l and the normal component of the dashpot force F_n^d, as expressed in Equations (1)–(3).

$$F_n^l = k_n g_c \tag{1}$$

$$F_n^d = \left(2\beta_n\sqrt{m_c k_n}\right)\dot{\delta}_n \tag{2}$$

$$m_c = \frac{m_1 m_2}{m_1 + m_2} \tag{3}$$

Here, k_n denotes the normal stiffness, g_c is the overlap (indentation) between two contacting particles, β_n is the normal critical damping ratio, m_1 and m_2 are the masses of the contacting particles, and $\dot{\delta}_n$ represents the relative normal translational velocity. The shear components of the linear force $\mathbf{F_s}$ is calculated as the sum of the linear shear force $\mathbf{F_s^l}$ and the dashpot shear force $\mathbf{F_s^d}$, as given in Equations (4)–(6).

$$\mathbf{F_s^l}(t) = \left(F_{ss}^l(t), F_{st}^l(t)\right) = \min(\|\mathbf{F_s^*}\|, \mu F_n^l)\frac{\mathbf{F_s^*}}{\|\mathbf{F_s^*}\|} \tag{4}$$

$$\mathbf{F_s^*} = \mathbf{F_s^l}(t - \Delta t) - k_s \Delta\boldsymbol{\delta_s} \tag{5}$$

$$\mathbf{F_s^d} = \left(F_{ss}^d, F_{st}^d\right) = \left(2\beta_s\sqrt{m_c k_s}\right)\dot{\boldsymbol{\delta}}_\mathbf{s} \tag{6}$$

In Equations (4)–(6), μ denotes the friction coefficient, k_s is the shear stiffness, $\Delta\boldsymbol{\delta_s}$ is the adjusted relative shear-displacement increment, and $\dot{\boldsymbol{\delta}}_\mathbf{s}$ represents the relative shear translational velocity. The rolling resistance moment $\mathbf{M_r}$ is calculated according to Equations (7)–(10).

$$\mathbf{M_r}(t) = \min(\|\mathbf{M_r^*}\|, \mu_r \bar{R} F_n^l)\frac{\mathbf{M_r^*}}{\|\mathbf{M_r^*}\|} \tag{7}$$

$$\mathbf{M_r^*} = \mathbf{M_r}(t - \Delta t) - k_r \Delta\boldsymbol{\theta_b} \tag{8}$$

$$k_r = k_s \bar{R}^2 \tag{9}$$

$$\bar{R} = \frac{R_1 R_2}{R_1 + R_2} \tag{10}$$

Here, μ_r is the rolling friction coefficient, k_r is the rolling resistance stiffness, $\Delta\boldsymbol{\theta_b}$ is the relative bend-rotation increment, and R_1 and R_2 are the radii of the two contacting particles.

2.3 *Calibration of contact model parameters*

The normal stiffness k_n was set to 3.3×10^4 N/m so that the compression index C_C, calculated using the void ratios at mean effective stresses of 50 and 100 kPa during normal consolidation, would be comparable to that of Toyoura sand. The shear stiffness k_s was set to 1.65×10^4 N/m such that the initial shear stiffness under monotonic shear would match the initial tangential stiffness observed in undrained shear tests on Toyoura sand with initial void ratios ranging from 0.732 to 0.752.

The range of friction coefficient μ has been reported to lie between 0.25 and 0.50, based on inter-particle loading tests (Senetakis et al., 2022) and previous DEM studies simulating shear behavior (Jiang et al., 2022). In the present study, after trial-and-error testing with reference to these works, μ = 0.36 was adopted. The rolling friction coefficient μ_r was set to 0.25, in accordance with previous DEM simulations of direct shear tests (Benmebarek and Rad, 2023). The normal critical damping ratio β_n was set to 0.45, and the tangential counterpart β_s was assigned the same value. This value corresponds to a restitution coefficient of 0.2, as used in previous DEM studies on liquefaction behavior (Banerjee et al., 2023). The calibrated parameters used in the contact model to represent the behavior of fine sand are summarized in Table 1.

Table 1. Parameters for the rolling resistance linear model.

Parameter	Symbol	Value	Unit
Normal stiffness	k_n	3.3×10^4	N/m
Shear stiffness	k_s	1.65×10^4	N/m
Friction coefficient	μ	0.36	-
Rolling friction coefficient	μ_r	0.25	-
Normal critical damping ratio	β_n	0.45	-
Shear critical damping ratio	β_s	0.45	-

3 MICROMECHANICAL RESPONSE UNDER CONSTANT-VOLUME CYCLIC SHEAR

The constant-volume cyclic shear tests were conducted on the specimen that had been consolidated under the mean effective stress of 100 kPa, with a cyclic stress ratio of 0.25. Figures 3 and 4 show the effective stress path and the stress–strain relationship, respectively. Points [a] to [e] in Figure 4 indicate the residual strain levels at which reconsolidation was performed, as referenced later in the discussion on anisotropy. The cyclic loading was terminated after ten cycles of shear stress amplitude. As shown in Figures 3 and 4, the recovery of effective stress and shear stiffness indicates the occurrence of cyclic mobility.

To evaluate the degree of sliding and rotation at inter-particle contacts, the indices P_s and P_r proposed by Kamura et al. (2026) were calculated as the proportions of sliding and rotating contacts relative to the total number of contacts. Figure 5 presents the relationship between P_s, P_r, and shear strain. During the phase where shear strain developed without the presence of shear stress (from 3% to –1% strain), P_s ranged from 45% to 60%, while P_r remained between 80% and 100%, indicating that rotation was more dominant than sliding. In the subsequent phase, where shear stress began to recover (from –1% strain onward), P_s stabilized around 45%, and P_r fluctuated between 75% and 80%. These observations suggest that the granular assembly exhibited cyclic mobility while maintaining a consistent ratio between sliding and rotation.

In addition to sliding and rotation, the stability of the contact structure was evaluated by computing the coordination number, defined as the average number of contacts per particle. Figure 6 shows the relationship between the coordination number and shear strain during constant volume cyclic shear. As seen in the figure, the coordination number decreased sharply from approximately 2.8–2.9 when shear stress was lost during unloading in the stress–strain response. Notably, when shear stress began to recover, the coordination number returned to the same level of 2.8–2.9, suggesting that particles formed a structurally stable condition with three-point contacts.

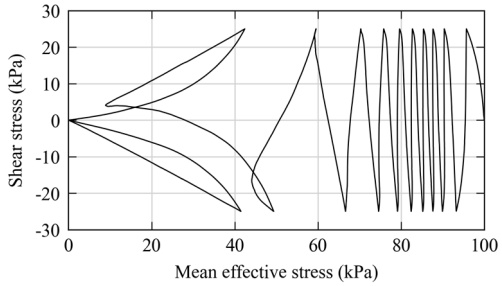

Figure 3. Effective stress path during constant-volume cyclic shear.

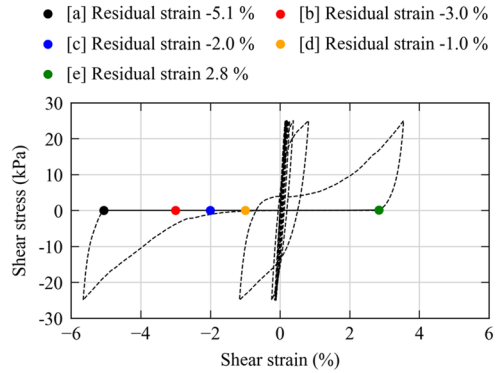

Figure 4. Stress–strain relationship during constant-volume cyclic shear.

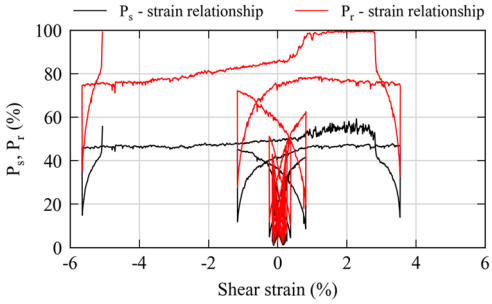

Figure 5. Proportion of sliding contacts P_s (black line) and rotating contacts P_r (red line) during constant-volume cyclic shear.

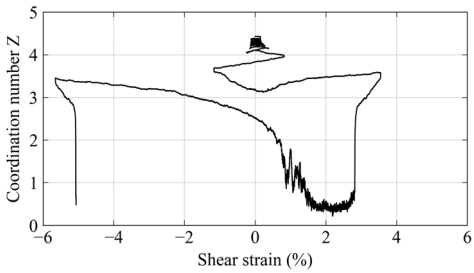

Figure 6. Relationship between coordination number and shear strain during constant-volume cyclic shear.

Furthermore, during the period in which strain continued to increase despite the absence of shear stress, the coordination number gradually increased. This indicates that the granular assembly exhibited cyclic mobility by forming a more stable contact structure while maintaining a constant balance between sliding and rotation, where particle rotation consistently dominated over sliding.

4 ANISOTROPY IN MONOTONIC SHEAR BEHAVIOR AFTER RECONSOLIDATION

To understand the development of anisotropy caused by constant-volume cyclic shear, the constant-volume monotonic shear tests were conducted on granular assemblies after initial consolidation (referred to as "consolidation") and after reconsolidation. Monotonic shear was applied in both the unloading direction at the end of cyclic shear (hereafter referred to as the "positive direction") and the opposite direction ("negative direction") up to shear strains of ±10%.

The reconsolidation was conducted on the specimen that had undergone constant volume cyclic shear with a residual strain of [a] –5.1%, as shown in Figure 4. The effective stress path and stress–strain behavior for the post-reconsolidation monotonic shear are presented in Figure 7. In the positive shear direction, effective stress and shear stress initially decreased and then recovered, whereas in the negative direction, both stresses continued to increase. The stress–strain curves also show a clear contrast: shear stress degradation was observed in the positive direction, while shear stress development was evident in the negative direction. These findings demonstrate that the granular assembly exhibited pronounced anisotropy after reconsolidation.

In addition to evaluating the anisotropy of the specimen after reconsolidation, a series of numerical simulations was conducted to investigate how variations in shear history at the end of constant volume cyclic shear affect the resulting anisotropy. Specimens were reconsolidated from different residual strain states and subjected to constant volume monotonic shear. As shown in Figure 4, shear was continued beyond the termination point of cyclic loading (point a), and specimens were extracted at residual strains of –3.0% [b], –2.0% [c], –1.0% [d], and +2.8% [e], followed by reconsolidation at each stage.

Figure 8 presents the effective stress paths and stress–strain responses during constant volume monotonic shear for specimens with different strain histories. The black line [a] in the figure corresponds to the data shown previously in Figure 8. Compared to the specimen reconsolidated at point [a], the specimen at point [b] exhibited a weaker degree of anisotropy. The specimen at point [c] displayed nearly isotropic behavior. At point [d], the direction of anisotropy was reversed, and at point [e], the reversed anisotropy was further intensified. These results indicate that anisotropy evolved continuously and systematically during the liquefaction process from point [a] to point [e]. This trend is consistent with the experimental findings of Yamada et al. (2010). Further, anisotropy was observed even when the residual shear strain was 0.0% (i.e., at the origin). The strain value at which anisotropy disappeared differed from the midpoint between the endpoints of the residual strain range (–5.1% and +2.8%), calculated as –1.15%. This indicates that anisotropy is not solely determined by the magnitude of residual shear strain.

To examine the macroscopic anisotropy observed in Figure 8 from a micromechanical perspective, Figure 9 shows the orientation distribution of contact planes in the zx-plane for the reconsolidated specimens at points [a], [c], and [e]. The specimen reconsolidated at point [a] exhibited a biased distribution of contact orientations in the ranges of 90–160° and

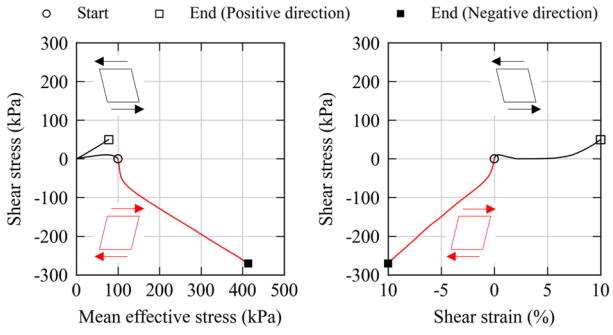

Figure 7. Monotonic shear behavior after cyclic shear loading.

270–340°. In contrast, the distribution at point [c] was nearly isotropic. The specimen at point [e] exhibited a shift in preferential contact orientation to the ranges of 10–100° and 190–280°. These results suggest that the contact structure evolved systematically during cyclic shear under constant volume conditions.

Considering that the major principal stress direction in positive shear is approximately 45° and 225°, and in negative shear is around 135° and 315°, it can be inferred that shearing aligned with directions of sparse contacts tends to be unstable and results in lower stiffness. Conversely, shearing in directions aligned with densely packed contacts leads to stable responses with higher stiffness. Therefore, the observed changes in anisotropy in the effective stress paths and stress–strain relationships can be attributed to changes in the contact structure.

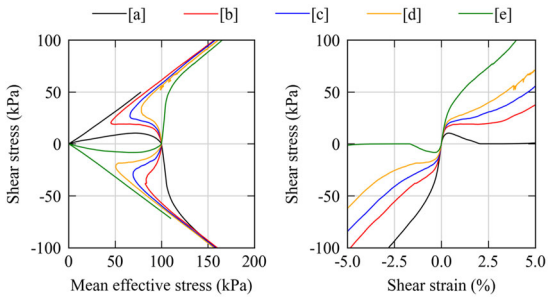

Figure 8. Constant volume monotonic shear behavior of specimens reconsolidated from different levels of residual strain.

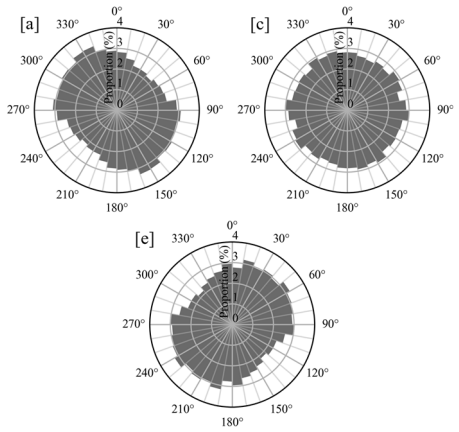

Figure 9. Circular histograms of contact plane orientation (in the zx-plane) after reconsolidation.

5 CONCLUSIONS

In this study, three-dimensional DEM simulations of constant volume cyclic shear were conducted to microscopically evaluate the undrained cyclic shear behavior of fine sand. The key findings obtained are summarized as follows:

- By calibrating the contact model parameters based on mechanical reasoning from consolidation and monotonic shear behavior, it was possible to reproduce the undrained cyclic shear response of fine sand.
- When the coordination number dropped below approximately 2.8–2.9 during cyclic shear, the contact structure became unstable, resulting in a loss of both effective stress and shear stress, accompanied by a sharp reduction in coordination number.
- In the phase where shear strain progressed without shear stress, particle rotation was more dominant than sliding at contacts.
- During the strain development phase under liquefaction, the coordination number increased beyond 2.8–2.9, while the proportion between sliding and rotation remained nearly constant. This transition to a stable contact structure contributed to the recovery of shear stiffness.

Furthermore, to evaluate the evolution of anisotropy in granular assemblies induced by constant volume cyclic shear, specimens were reconsolidated from various levels of residual strain and subjected to constant volume monotonic shear in both positive and negative directions. The findings are summarized as follows:

- The anisotropy observed in the effective stress paths and stress–strain relationships after reconsolidation changed continuously and systematically depending on the residual strain history imposed by cyclic shear.
- Anisotropy was also observed at a residual shear strain of 0.0% (the origin). The strain level at which anisotropy disappeared differed from the midpoint between the endpoints of the residual strain range (–5.1% and +2.8%), calculated as –1.15%. This indicates that anisotropy is not solely determined by the magnitude of residual shear strain.
- The directional distribution of contact numbers changed systematically with residual strain. Specimens exhibited weaker responses when the major principal stress was oriented toward directions with fewer contacts and more stable responses when aligned with directions of greater contact density.

6 ACKNOWLEDGEMENTS

This research was supported by JSPS KAKENHI (Nos. 24K00974, 24K00975, and 25K01327).

7 REFERENCES

Banerjee, S, K., Yang, M., and Taiebat, M. 2023. Effect of coefficient of uniformity on cyclic liquefaction resistance of granular materials. *Computers and Geotechnics*, 155, 105232.

Benmebarek, M, A., and Rad, M, M. 2023. Effect of Rolling Resistance Model Parameters on 3D DEM Modeling of Coarse Sand Direct Shear Test. *Materials*, 16, 2077.

Itasca Consulting Group, Inc. 2024. PFC 7.0.

Iwashita, K., and Oda, M. 1998. Rolling Resistance at Contacts in Simulation of Shear Band Development by DEM. *Journal of Engineering Mechanics*, 124(3), 285-292.

Jiang, M., Kamura, A., and Kazama, M. 2021. Comparison of liquefaction behavior of granular material under SH- and Love-wave strain conditions by 3D DEM. *Soils and Foundations*, 61(5), 1235-1250.

Jiang M., Kamura, A., and Kazama, M. 2022. Numerical study on liquefaction characteristics of granular materials under Rayleigh-wave strain conditions using 3D DEM. *Soils and Foundations*, 62 (4), 101176.

Kamura, A., Shibata, T., Chiba, Y., and Yamada, S. 2026. Microscopic investigation of anisotropy induced by liquefaction history in fine sand using DEM. *Soil Dynamics and Earthquake Engineering*, 201, 109977.

Senetakis, K., Coop, M, R., and Todisco M, C. 2022. The inter-particle coefficient of friction at the contacts of Leighton Buzzard sand quartz minerals. *Soils and Foundations*, 53(5), 746-755.

Yamada, S., Takamori, T., and Sato, K. 2010. Effects on reliquefaction resistance produced by changes in anisotropy during liquefaction. *Soils and Foundations*, 50(1), 9-25.

Yamada, S., Okada, M., Nakano, M., Noda, T. 2023. Experimental study on sand anisotropy using hollow cylinder apparatus. *Soils and Foundations*, 63(3), 101326.

Yang, M., Taiebat, M., and Radjaï, F. 2022. Liquefaction of granular materials in constant-volume cyclic shearing: Transition between solid-like and fluid-like states. *Computers and Geotechnics*, 148, 104800.